

# Wavefront Measurement for EUV Lithography System through Hartmann Sensor

A. Polo, F. Bociort, S.F. Pereira, H.P. Urbach

Delft University of Technology, Department of Imaging Science and Technology,  
Optics Research Group, Lorentzweg 1, Delft, 2628CJ, The Netherlands;

## ABSTRACT

Accurate wavefront aberration measurement are essential for next-generation Extreme Ultraviolet (EUV) Lithography. During the past years several accurate interferometric techniques have been developed, but these techniques have limitation. In this work we discuss a different technique based on the Hartmann Wavefront Sensor that requires no interferometry. We present a mathematical model of this system and describe our experimental setup which demonstrates the feasibility and advantages in terms of dynamic range and accuracy compared to interferometric techniques.

**Keywords:** EUV lithography, adaptive optics, wavefront sensing

## 1. INTRODUCTION

Optical Projection Lithography (OPL) is presently the most widespread technology to print a geometrical pattern on a semiconductor wafer. The latest systems use deep-ultraviolet (DUV) radiation with a wavelength of 193 nm to transfer the pattern from a photo mask to a light-sensitive photo resist through a refractive optical system with a reduction factor of 4. Because of the continuing demand for more powerful and smaller chips, the semiconductor industry needs to develop new lithography machines that are capable of printing smaller feature sizes to increase the number of transistors on a semiconductor wafer. For a lithography system, the smallest feature size that can be printed (the critical dimension) and depth of focus of the system are given by

$$CD = k_1 \frac{\lambda}{NA} \quad DOF = k_2 \frac{\lambda}{(NA)^2} \quad (1)$$

where  $k_1$  and  $k_2$  are experimental parameters,  $\lambda$  is the wavelength and  $NA$  is the numerical aperture of the system, i.e. both CD and DOF increase with the wavelength used to carry out the imaging and decrease with the numerical aperture of the system. Because the latest generation of OPL uses immersion to increase the  $NA$  of the system up to the value of 1.44, it is straightforward to think on the decrease of the wavelength to achieve a smaller resolution value.

Extreme Ultraviolet Lithography (EUVL) is considered as the next generation of pattern technology after the current immersion OPL. Since it uses photons of 13.5 nm wavelength to carry out the imaging, it is suitable for addressing not only the 32 nm half-pitch nodes but also several nodes beyond that.<sup>1</sup> However, material properties for the EUV range make this technique completely different from present-day lithography. EUV radiation, is strongly absorbed in all materials and gases and therefore Multilayer (ML) aspherical mirrors have to be used in the projection optics as shown schematically in Fig.1. Moreover, because of the partial reflectivity of a ML mirror (about 70%), part of the radiation is absorbed by the ML mirrors and cause deformation of the mirror's surface. This can cause aberrations in the EUV beam resulting in a loss of resolution and consequently in a poor image projected on the wafer. In order to minimize such systematic errors in a EUVL system an option is to introduce an adaptive optics system to correct the aberrations in the EUV mirror system and achieve a high-quality diffraction limited imaging, like in an astronomic telescope. Therefore, a significant amount of research is done to develop metrology techniques that can measure the wavefront at such short wavelength with a very high accuracy.<sup>2,3</sup>

In this paper we report the simulation and the first experimental results of an Hartmann Wavefront Sensor (HWFS) design for EUV as an instrument to detect aberrations in a EUV Lithography machine. In particular,

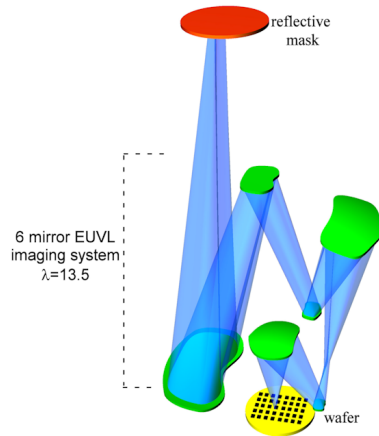


Figure 1. EUV Lithography system consisting of six mirrors image the reflective mask onto a wafer.

in Section 2 we describe its working principle, the theory on which the simulation is based and the simulation results. In Section 3 we describe the design of our experimental setup and the first experimental results. Finally, in Section 4, the conclusion and the future works are presented.

## 2. THEORY AND SIMULATION RESULT

It is well known that interferometry is the most accurate metrology technique for wavefront characterization. It has been shown that it can achieve accuracy in aberration detection of the order of  $\lambda/350$  with  $\lambda = 13.5\text{nm}$  but it requires significant effort to calibrate the system and to analyze the data. Moreover, it is limited by the temporal and spatial coherence of the beam under test, and high-magnitude aberrations are very difficult to be measured.

Hartmann (HWFS) and Shack-Hartmann (S-HWFS) Wavefront Sensors are already successfully applied for real time wavefront characterization in a wide range of the electromagnetic spectrum from infrared to ultraviolet. These sensors allow simultaneous measurement of both phase and intensity distribution at the same time. Moreover aberration of widely different magnitudes can be detected with these techniques.<sup>4</sup>

### 2.1 Hartmann Wavefront Sensor principle

In the S-HWFS the beam under test is sampled by a micro-lens array placed in the beam path. The individual beams are collected by a detector placed at the focal plane of the micro-lenses. Aberrations in the beam cause a deviation of the sampled beam which results in a measurable shift of the individual spot with respect to the aberration-free case. This shift can be transformed into the local slope of the wavefront from which the whole wavefront can be reconstructed. Due to the strong absorption of EUV radiation in all materials, this technique using a micro-lens array is not suitable for this spectral range.

In the HWFS (Fig.2) the micro-lens array is replaced by a hole array placed in the beam path. Because of the absence of the lenses, the resolution in the spots detection and therefore in the aberration detection decreases.

The different holes in the grid are labeled by two indices  $i$  and  $j$ , associated with the  $x$  dimension and  $y$  dimension respectively. For each hole, the local slopes of the wavefront, denoted by  $S_{ij}^x$  and  $S_{ij}^y$ , are given by the following equations:

$$\begin{cases} S_{ij}^x = \frac{\partial W}{\partial x} = \frac{x_{c,ij} - x_{r,ij}}{L} \\ S_{ij}^y = \frac{\partial W}{\partial y} = \frac{y_{c,ij} - y_{r,ij}}{L} \end{cases} \quad (2)$$

where:

- $(x_c, y_c)$  and  $(x_r, y_r)$  are the positions of the measured and reference spot, respectively;
- $L$  represents the distance between the sampling and detection planes.

From the complete mapping of the wavefront gradient  $S_{ij}^x$  and  $S_{ij}^y$  the wavefront is reconstructed in a modal approach using the Zernike polynomials.<sup>5</sup>

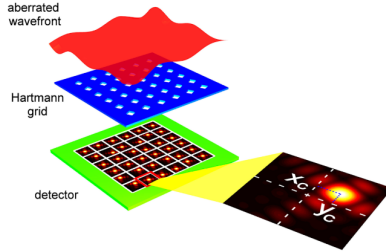


Figure 2. HWFS scheme

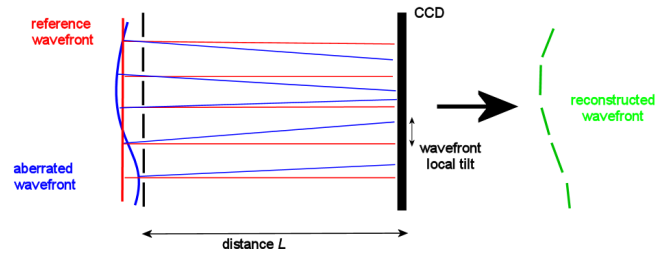


Figure 3. HWFS working principle

The hole size and the distance  $L$  are chosen such that overlap in the projected pattern is avoided. The position of each spot is calculated by a center of mass algorithm.<sup>6</sup> Depending on the geometrical properties of the beam that is analyzed and the desired performance of the sensor, the size of the hole in the array of the Hartmann grid can vary with hole with diameter from  $30 \mu\text{m}$  to  $120 \mu\text{m}$  and with hole spacing from  $60 \mu\text{m}$  to  $300 \mu\text{m}$  for  $\lambda=13.5\text{nm}$ .

Note that with the described approach, the whole wavefront is reconstructed as stitching of the local tilt wavefront in the sampling hole array (Fig.3). Therefore the information about the curvature of the local wavefront is lost and this causes loss of resolution in the wavefront reconstruction. We will describe elsewhere an algorithm to measure this additional information and to overcome this limitation of resolution.

## 2.2 Simulation

In our simulation, the Hartmann grid in the  $z = 0$  plane consists of an array with  $44 \times 44$  holes over an  $11 \times 11 \text{mm}^2$  area. The holes are squares with  $80 \mu\text{m}$  size, spaced by  $225 \mu\text{m}$ . Each hole is rotated by 25 degree in order to minimize the overlap of the diffraction orders from the adjacent holes in the measurement plane.<sup>7</sup> The distance  $L$  between the grid and the image plane is set to 400 mm. The wavelength is 13.5 nm.

The aberration in the system is introduced as a phase distortion factor (in terms of a Zernike polynomial) that multiplies the Hartmann grid function according to the following equation:

$$U(x, y, 0) = U_0 \exp[ikW(x, y)]G(x, y) \quad (3)$$

where:

- $U(x, y, 0)$  is the complex field distribution across the  $z = 0$  plane;
- $W(x, y)$  is the aberration;
- $k = 2\pi/\lambda$  is the wave number;
- $G(x, y)$  is the transmission function of the Hartmann grid (i.e.  $G$  is 1 inside the holes and 0 between the holes).

The intensity distribution in the detector plane  $U(x, y, L)$  at a distance  $L$  is calculated by propagation in free space of the angular spectrum  $A(f_x, f_y, 0)$  of  $U(x, y, 0)$ :

$$U(x, y, L) = \iint_{-\infty}^{+\infty} A(f_x, f_y, 0) \exp \left[ j \frac{2\pi}{\lambda} \sqrt{1 - f_x^2 - f_y^2} L \right] \exp[j2\pi(f_x x + f_y y)] df_x df_y \quad (4)$$

where  $f_x$  and  $f_y$  are the spatial frequencies in the Fourier domain.<sup>8</sup>

Figure 4 and 5 show the simulation for the intensity distribution at the object plane ( $z = 0$ ) and at the image plane ( $z = L$ ).

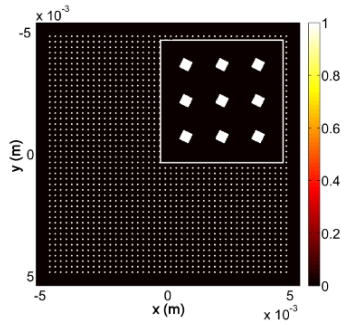


Figure 4. Intensity distribution at the Hartmann Wavefront Sensor. Inset is an enlarged detail.

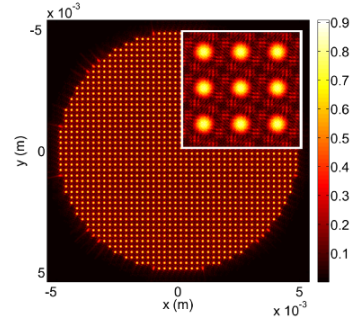


Figure 5. Intensity distribution at a distance  $L$  from the Hartmann Wavefront Sensor. Inset is an enlarged detail.

### 2.3 Simulation results

In order to show the advantages of our algorithm in the aberration reconstruction a comparison between our algorithm and a spot detection based on the center of mass algorithm is made. We simulate different kinds of aberrations, namely defocus, astigmatism, coma and a mix of them and then we compare the reconstructed wavefront with the simulated one for both algorithms. Finally we evaluate the root mean square (rms) error for the reconstructed wavefront.

The following figures show the result of the simulations. In particular, Figure 6 shows the spatial distribution of  $W(x, y)$  for the different aberrations; Figure 7 and 8 show the aberration mismatch between the simulated and the reconstructed aberrations for both algorithms. Finally Table 1 lists the respective rms error.

The results of the simulations prove that with our algorithm we achieve an improvement in the reconstruction of the wavefront from the diffracted image intensity with a resolution about 10 times better compared to the center of mass algorithm. In particular, the simulations show that the absolute rms error in the reconstructed wavefront with respect to the simulated one is about  $\lambda/90$  for  $\lambda = 13.5\text{nm}$  making this technique a valid alternative to interferometry.

Table 1. rms error for the reconstructed wavefront for two different reconstruction algorithms

	Defocus	Astigmatism	Coma	Cocktail
RMS error (center of mass algorithm)	1.35 nm	1.11 nm	0.94 nm	1.2 nm
RMS error (New algorithm)	0.16 nm	0.26 nm	0.095 nm	0.19 nm

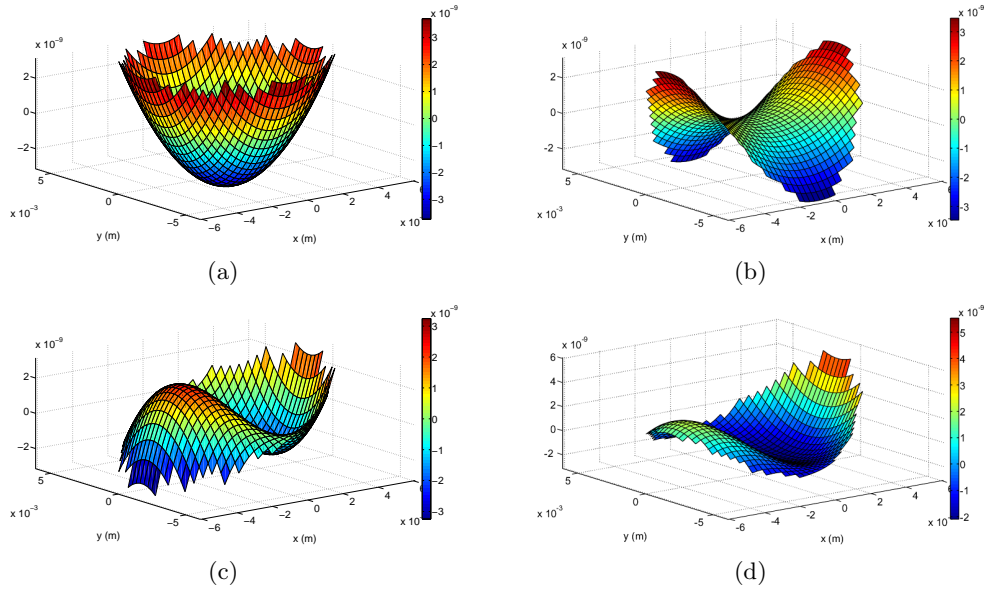


Figure 6. aberration simulation. a) defocus, b) astigmatism c) coma and d) arbitrary aberration

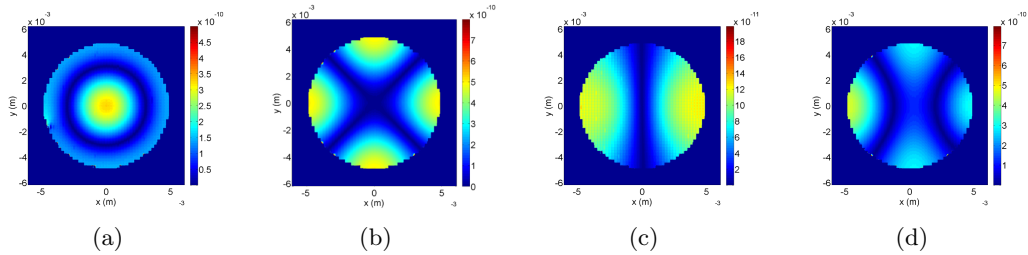


Figure 7. Aberration mismatch of the reconstructed wavefront compared to the simulated one with the new reconstructed algorithm for the following aberration type: a) defocus, b) astigmatism, c) coma, d) arbitrary aberration.

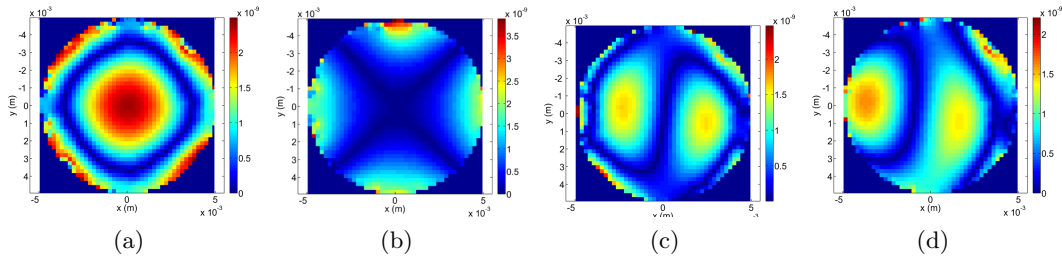


Figure 8. Aberration mismatch of the reconstructed wavefront compared to the simulated one with a reconstructed algorithm based on the spot center of mass for the following aberration type: a) defocus, b) astigmatism, c) coma, d) arbitrary aberration.

### 3. EXPERIMENTAL SETUP

In order to give an experimental proof of principle of our method we present the design of an experimental setup in the visible range using a red light. We use a semi-conductor intensity stabilized laser with wavelength  $\lambda=638$  nm. All parameters in the setup have been scaled according to this new wavelength so that we have the same Fresnel Number  $F_n = d^2/\lambda z$ , where  $d$  is the size of the hole in the Hartmann array,  $\lambda$  the wavelength and  $z$  the distance between the Hartmann array and the detector. The new parameters as well as the parameters for the EUV case are listed in the Table 2.

Table 2. comparison between the experimental parameter for EUV and visible range

	EUV setup	Visible setup
Wavelength $\lambda$ (nm)	13.5	638.8
Hole size ( $\mu\text{m}$ )	80	200
Hole pitch	225	562.5
Hartmann mask - detector distance (mm)	400	50

Figure 9 shows the sketch of our experimental setup.

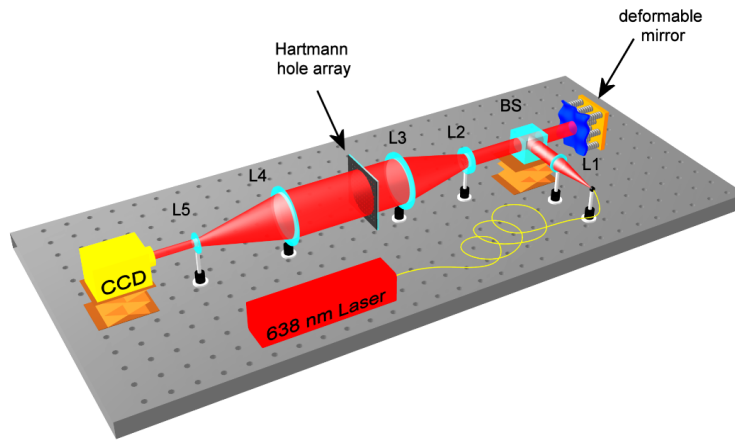


Figure 9. Experimental setup

The beam from an optical fiber is first collimated by the lens  $L1$ . A beam splitter splits the beam to a deformable mirror used to generate the desired aberration and then the beam is expanded by a factor 8.3 by the lenses  $L2$  and  $L3$  in order to illuminate uniformly at the whole Hartmann grid. The diffraction pattern resulting after the propagation of the beam through the holes array is demagnified by a factor of 7.5 by the lenses  $L4$  and  $L5$  in order to fit into the CCD camera ( $1280 \times 960$  pixels). The lens specifications are described in Table 3.

Table 3. lens specification

Lens	Focal distance (mm)	Diameter (inch)
L1	+40	1
L2	+30	1
L3	+250	2
L4	+150	2
L5	+20	$\frac{1}{2}$

The Hartmann grid consists of a plate of glass 1.5 mm thick. On top of the plate  $200\mu\text{m}$  of Chromium are deposited on it and then the hole array geometry has been made by electron beam lithography. Figure 10 shows the recorded diffraction pattern at a distance of 50 mm from the Hartmann grid.

As we can see each spot is clearly resolved in accordance with the simulation showed in Figure 5. This data can be used as input in our algorithm as showed in Section 2.3 to retrieve the wavefront in this real case.

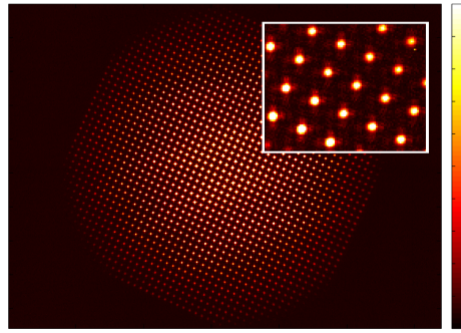


Figure 10. measured diffraction pattern at 50 mm distance from the Hartmann grid

#### 4. CONCLUSION

The purpose of this research is to investigate the advantages and possible constraints in the characterization of the wavefront using an Hartmann Wavefront Sensor working at 13.5 nm to be used in a EUV Lithography system. We are developing a new algorithm for the reconstruction of the aberration from an intensity pattern using an Hartmann grid. Simulations show the feasibility and the improved resolution of this new algorithm in the aberration reconstruction. An experimental setup in order to prove the principle of our simulation has already been designed and data analysis are currently under development.

#### 5. ACKNOWLEDGEMENT

This research is supported by the Dutch Ministry of Economic Affairs and the Provinces of Noord-Brabant and Limburg in the frame of the "Pieken in de Delta" program. We also want to thank Anja van Langen from the Kavli Nanolab and Vladimir Kutshoukov from the Charge Particle Optics department for manufacturing the Hartmann mask and Imagine Optics for the access to the patent n. Eur 1415133 - US 7,255,442 - Jap 4212472.

#### REFERENCES

- [1] Bjorkholm, J. E., "EUV lithography - the successor to Optical Lithography," *Intel Technology Journal Q3* (1998).
- [2] Bjorkholm, J. E., MacDowell, A. A., and Wood, O. R., "Phase-measuring interferometry using extreme ultraviolet radiation," *American vacuum Society* **13**, 2919–2922 (1995).
- [3] Naulleau, P. P., Goldberg, K. A., and Lee, S., "EUV phase shifting PDI: a wavefront metrology tool with subangstrom reference-wave accuracy," *Applied Optics* **38**, 7252–7263 (1999).
- [4] Mercere, P., Zeitoun, P., and Idir, M., "Hartmann wavefront measurement at 13.4 nm with  $\lambda_{EUV}/120$  accuracy," *Optics Letter* **28**, 1524–1536 (2003).
- [5] Southwell, W. H., "Wavefront estimation from wavefront slope measurement," *JOSA* **70**, 998–1006 (1980).
- [6] Carvalho, L. A., "A simple and effective algorithm for detection of arbitrary hartmann-shack patterns," *Journal of biomedical informatics* **37**, 1–9 (2004).
- [7] with the authorization of Imagine Optics, patent n. Eur 1415133 - US 7,255,442 - Jap 4212472.
- [8] Goodman, J. W., [*Fourier Optics (3rd edition)*], Roberts and Company, New York (2004).